A Decomposition Approach to Cyclostratigraphic Signal Processing SUPPLEMENTARY MATERIALS

Sébastien Wouters[1,2], Michel Crucifix[3], Matthias Sinnesael[4], Anne-Christine Da Silva[1], Christian Zeeden[5], Miroslav Zivanovic[6], Frédéric Boulvain[1], Xavier Devleeschouwer[2]

1 Sedimentary Petrology, Liege University, Allée du Six Août 12, 4000 Liège, Belgium
2 O.D. Earth and History of Life, Royal Belgian Institute of Natural Sciences, 29 rue Vautier, 1000 Brussels, Belgium
3 Earth and Life Institute, UCLouvain, Place Louis Pasteur 3, Louvain-La-Neuve, 1348, Belgium
4 Department of Earth Sciences, Mountjoy Site, Durham University, South Road, Durham DH1 3LE, UK
5 LIAG – Leibniz Institute for Applied Geophysics, Geozentrum Hannover, Stilleweg 2, 30655, Hannover, Germany
6 Electrical Engineering Department, Public University of Navarra, Campus Arrosadía s/n, 31006 Pamplona, Spain

Correspondence to: Sébastien Wouters (wouterseb@gmail.com)

8 Ratio spectra of low-frequency dominated noise

We briefly discussed the behaviour of white noise in the ratio population plot (section 4.3). White noise, however, is not the only kind of noise to consider; more typically, as we discuss in section 6.2, climatic variations are pervasively affected by low-frequency dominated noise. We are currently unable to provide a state-of-the-art report on how all possible noise models behave in our decomposition methodology. Still, to provide a glimpse into how climatic noise behaves in decompositions, we discuss here the frequency ratio behaviour of a simple low-frequency dominated artificial noise model. The noise model we will be using is the first-order autoregressive 'AR(1)' process (e.g., Mann and Lees 1996):

$$r_n = \rho r_{n-1} + w_n$$

where n is the time stamp, going from 1 to N (the amount of data points) with an increment of 1, r_n is the noise sequence, ρ is the lag-one autocorrelation coefficient (it is a constant that can be set from 0 to 1), and w_n is a white noise sequence with a given variance. Obviously, if ρ is set at 0, the output will be the w_n white noise sequence. For our purpose, we chose to set ρ at 1, i.e. the other extreme, to explore noise highly dominated by low-frequency components.

We thus decompose, using the extricate algorithm, a 3000 point AR(1) sequence having a ρ lag-one autocorrelation coefficient of 1 (Fig. SF1). We extract 10 components, the last being a linear trend. The 8th and 9th components have abnormally low amplitude compared to the expected increase of amplitude with higher period/lower frequency tendency observed in the 7 components before (Fig. SF1; see also Flandrin et al., 2004 and Rilling et al., 2005). We hypothesise that this effect can be ascribed to instabilities at the end of the signal, which would in general be heavily pronounced in the antepenultimate and penultimate components of a decomposition, considering the linear trend as last component (and considering that the components are ordered from high to low frequency). This is for the reason that, in practice, the antepenultimate and penultimate components will in all

likeliness only display 2 or 1 cycle(s), and that these will include the end of the signal; they can thus easily be missing a part, thereby truncating them and reducing their amplitude. In contrast, the higher frequency components (with periods going from 1 to 500) have punctual occurrences of high amplitude cycles, again attributed to the ends of the signal (Fig. SF1), which account for the "missing amplitude" in lower frequency components.

Figure SF1: Spectral population plot of a 3000 point red noise signal.

Notwithstanding the end-of-signal problems, the general behaviour of our low-frequency dominated sequence in the ratio population plot (Fig. SF2) is comparable to what is observed in the white noise signal (section 4.3). Each pair of successive component approaches a ratio of 2 (Fig. SF2B), which is again coming from the dyadic nature of EMD and EEMD methodologies (and of modally meaningful decomposition in general). Similarly to white noise, in the whole ratio spectrum, the square root of ratio power peaks around a ratio of 2 and steadily decreases towards higher ratios (Fig. SF2A). This is typical of a decomposition where amplitude depends on the frequency, and can be maximised at a certain frequency range (the first component in white noise, the last component where amplitude is at least partly unaltered by end-of-signal problems in low-frequency dominated noise). This, in turn, forms a continuum in the ratio spectrum. Therefore any break of the continuum could be symptomatic of non-noise processes.

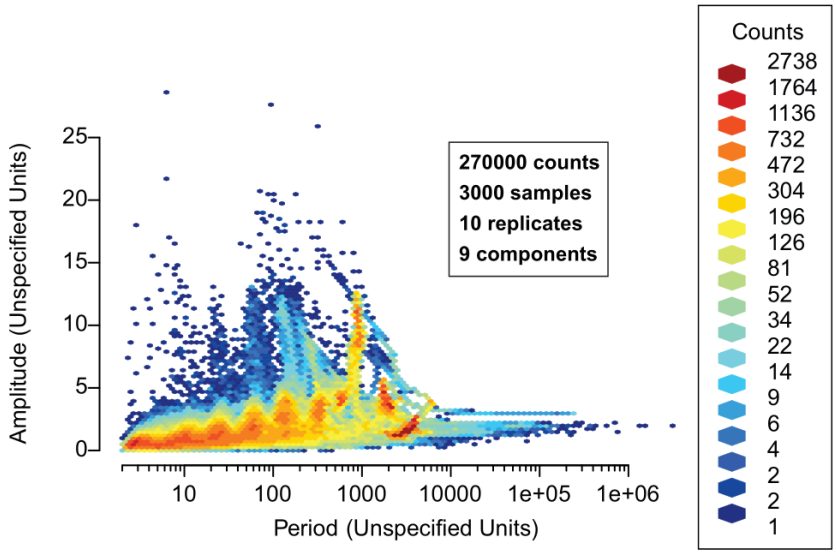

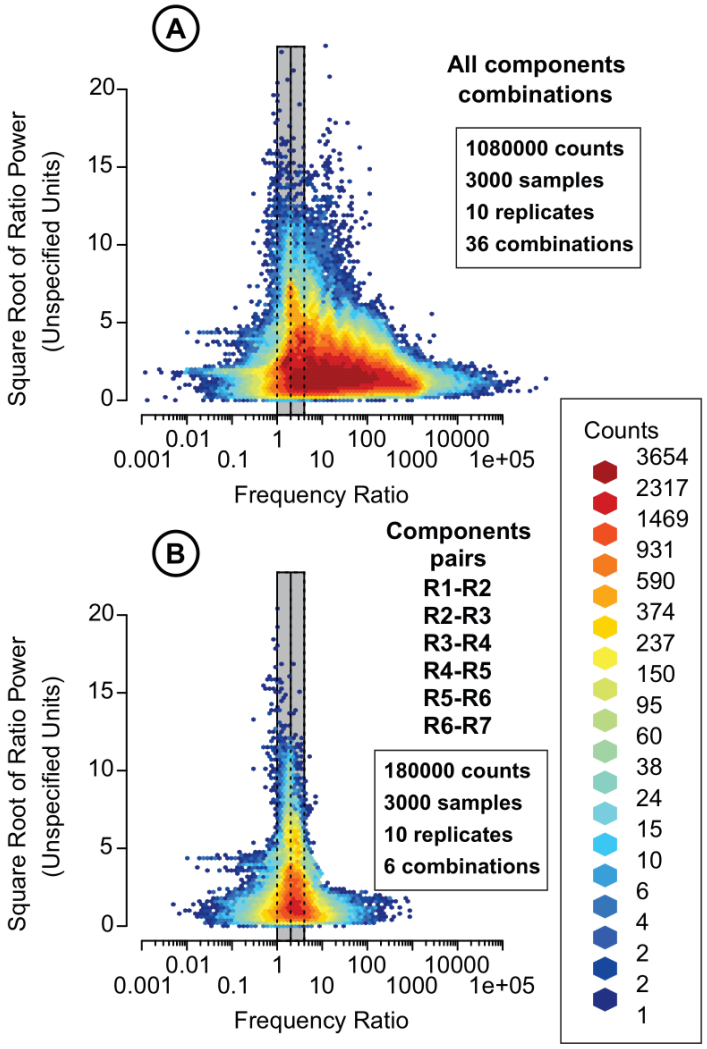

Figure SF2: (A) Ratio population for all pairs of components, of the same 3000 points red noise signal used for fig. SF1 (ensemble of 10 decompositions with identical parameters but with different white noise realisations). (B) Ratio population plot of the red noise signal for only the successive components. The grey rectangle delimits frequency ratios between 1 and 4, and is centred on a ratio of 2.

9 Additional case study: the CIP1 artificial signal

The CIP1 case study is an artificial signal generated for the Cyclostratigraphy Intercomparison Project (CIP). It was designed to contribute to the discussion on reproducibility in cyclostratigraphy (Sinnesael et al. 2019).

The CIP1 case study consists of a colour image of a supposed core that we converted into a greyscale raster (Fig. SF3A), in which the levels of grey could be coded numerically into greyscale arbitrary units that were averaged horizontally to obtain a numerical signal (Fig. SF3B). The greyscale raster and the converted signal are provided in the DecomposeR package. The astronomical signal at the source of CIP1 is the 21st of July insolation curve as calculated by Laskar et al. (2004) at 55°N between 8000 and 6000 ka. The insolation values are varying between 409 and 518 W.m^{-2}. To make the CIP case study, a constant value of 440 W.m^{-2} was removed from the insolation signal, and the result was squared (Sinnesael et al. 2019). This was meant to represent a threshold effect,

and resulted in breaking the symmetry of the signal (see the description of Fig. SF3B). The signal was then converted into 5 lithology classes to generate the artificial core image, and a stratigraphic depth was computed, with each lithology having a specific sedimentation rate (Sinnesael et al. 2019). The sedimentation rate is set to be higher in the lithologies corresponding to darker levels of grey (i.e.at the lower greyscale unit values). The length of the entire core was given as 26.38 metres. As the signal covers 2000 kyr, the average sedimentation rate of the entire record is of 0.01319 meters per kyr, which corresponds to 75.81 $kyr.m^{-1}$.

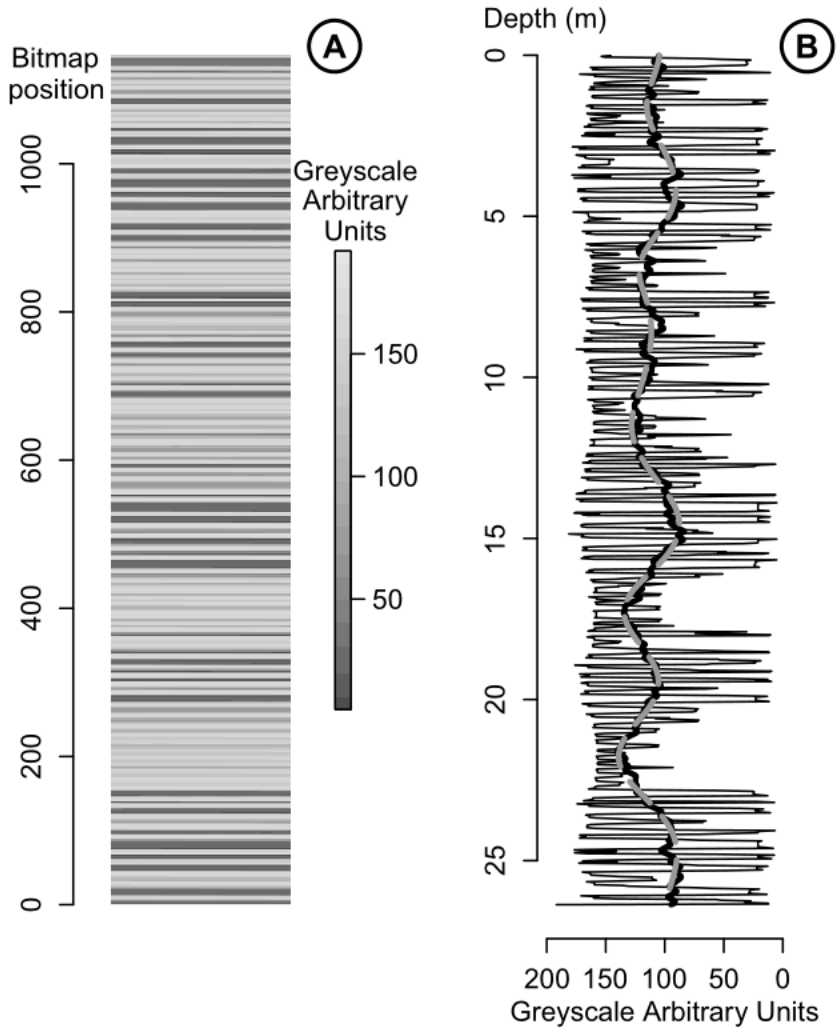

Figure SF3: (A) grey-scale version of the CIP1 original signal (image of a supposed core) and (B) its conversion into a proxy record, to which is added a running average of 101 points (bold black line) and an addition of some of the last components obtained via EEMD by "extricate" (bold grey dashed line). These two lines illustrate that the dissymmetry of amplitude modulation translates into raw cycles being poured into the signal by partial rectification (see also section 5.3.1 in Weedon 2003).

We use here an artificial case -for which the processes leading from the astronomical curve to the actual signal are known- to push as far as possible the extraction of any meaningful signal via decomposition and filtering. This can be done based on the knowledge of the sedimentation rate and of the periods of the cycles present in the

signal. The relevant cycles in the signal can be uncovered using periodograms of the insolation solution used to construct the case study, and the direct demodulation of the climatic precession solution (by direct we mean without any prior filtering or decomposition), as the climatic precession is the main cycle expressed in the insolation solution (Fig. 17).

10 Results

10.1 CIP1

The CIP1 signal (Fig. SF3) is decomposed in 8 components (Fig. SF4) using "extricate", which took less than 10 seconds on a standard workstation. The 8 components are named comp. 1 to 7, and "linear trend" (or lin. trend); we consider that comp. 7 is a cyclically-connoted residual. Ten replicates of the decomposition are performed, all of them are an average of 300 realisations, with each realisation having white noise added to them. The added white noise is uniformly distributed between -50 and 50 greyscale arbitrary units (which are the intensity units of the CIP1 signal in our proxy record). For comparison, the signal values are ranging between ca. 5 and 192 greyscale arbitrary units. The white noise intensity is chosen high enough to avoid mode mixing and to reduce the occurrence of riding waves, which are both checked on a visual basis. The sifting is not iterated (i.e. sifting number = 1) to avoid any smoothing of the amplitude of the components. This setting helps to preserve the amplitude modulation of comp. 2. The amplitude of comp. 2 is determined using the normalisation scheme of Huang et al. (2009), and is used to further study the cyclicity in the amplitude modulation (Fig. SF5). Decomposition is performed on the amplitude demodulation of comp. 2, extracting 8 components, named comp. 2’ to 8’, and "linear trend’", with comp. 8’ considered as a cyclically-connoted residual. We use the apostrophe (’) as a convention for the decomposition that comes from the demodulation. For visualisation purposes, the comp. 2 replicate used for demodulation is provided in 10 identical replicates in the distribution plots of the amplitude decomposition, and called comp. 1’. The demodulation decomposition is performed using "extricate": Ten replicates are computed, all made of a combination of 100 white-noise added realisations, with the sifting number set at 1. The added white noise is uniformly distributed between -100 and 100 greyscale arbitrary units, based on the same rationale than the decomposition on the raw signal.

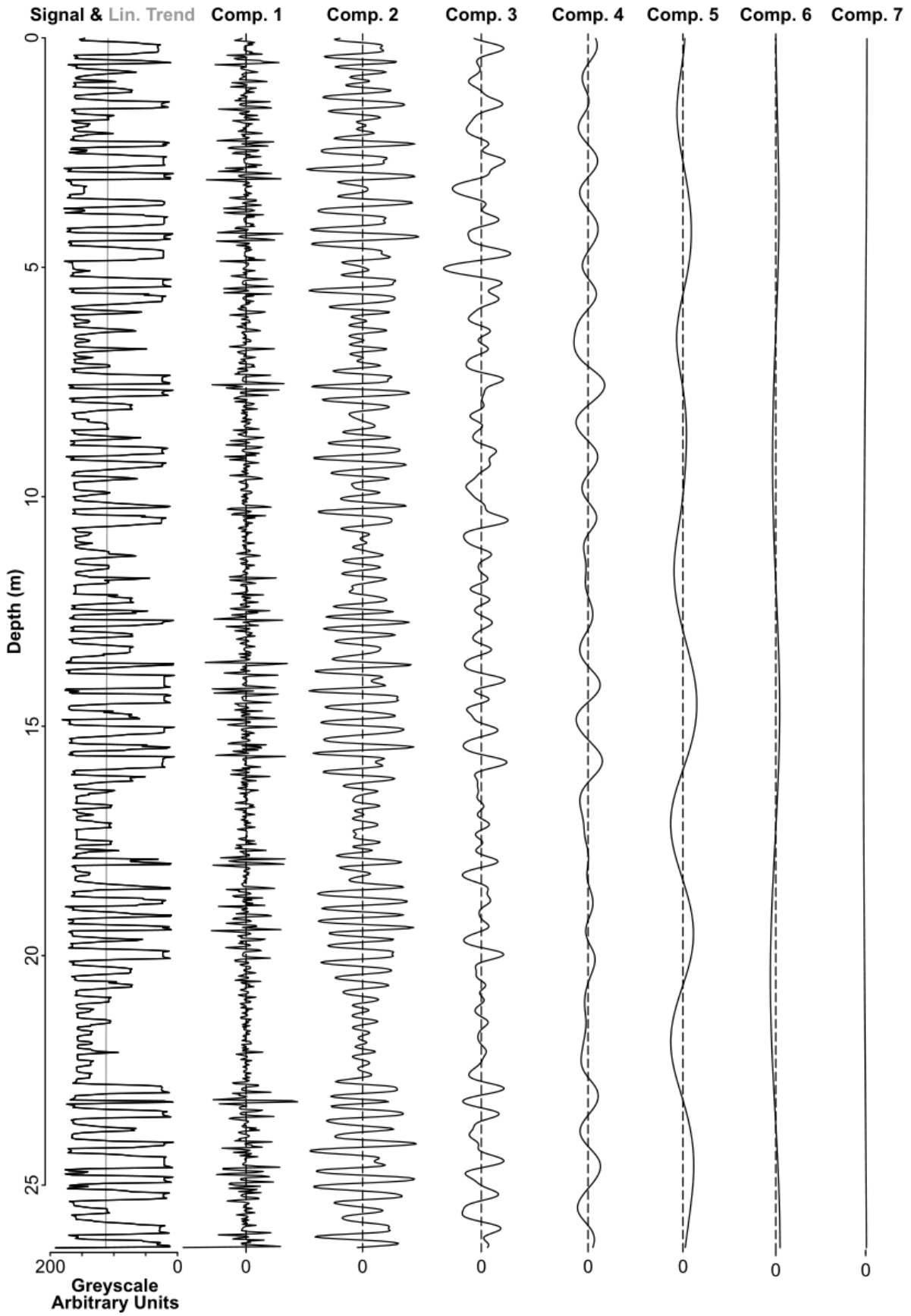
Signal & Lin. Trend
Comp. 1
Comp. 2
Comp. 3
Comp. 4
Comp. 5
Comp. 6
Comp. 7
Depth (m)
0
5
10
15
20
25
200
0
Greyscale
Arbitrary Units

Figure SF4

Figure SF4: EEMD decomposition the CIP 1 signal. The intensity scale of the components is identical to that of the initial signal. The linear trend (grey line) is part of the decomposition. Comp. (component) 2 displays strong and rhythmic amplitude modulation that is paralleled by the expression of comp. 4 and 5. These can be linked to the expression of climatic precession (ca. 23 kyr period), short and long eccentricity (observed here at ca. 125 and 405 kyr). This is coherent with eccentricity being a modulator of the expression of climatic precession. The other components are discussed in the text.

To compare our decomposition methodology to a conventional filtering approach, the CIP1 signal is also filtered on the expected climatic precession and obliquity frequencies with a Taner filter (Fig. SF6 and SF7), using the Astrochron package in R (Meyers, 2014). The filtering is performed after removal of the mean of the signal, with cut-off frequencies corresponding to the 15 and 30 kyr periods (considering a 75.81 $kyr.m^{-1}$ inverse sedimentation rate) for climatic precession and to the 35 and 70 kyr periods for obliquity. The choice of the cut-off frequencies was to obtain IMF-like filters with as much intensity as possible, which was checked for on a visual basis. We refer to these filtered results as the CIP1 23 kyr filter and the CIP1 40 kyr filter, respectively (Fig. SF4 and SF5). The other Taner filter parameters remained at default values (zero padding with 2 times the initial number of points, roll-off rate of 1000 dB per octave). The R script for all time-series analysis performed on the CIP1 signal is available as supplementary material SC4.

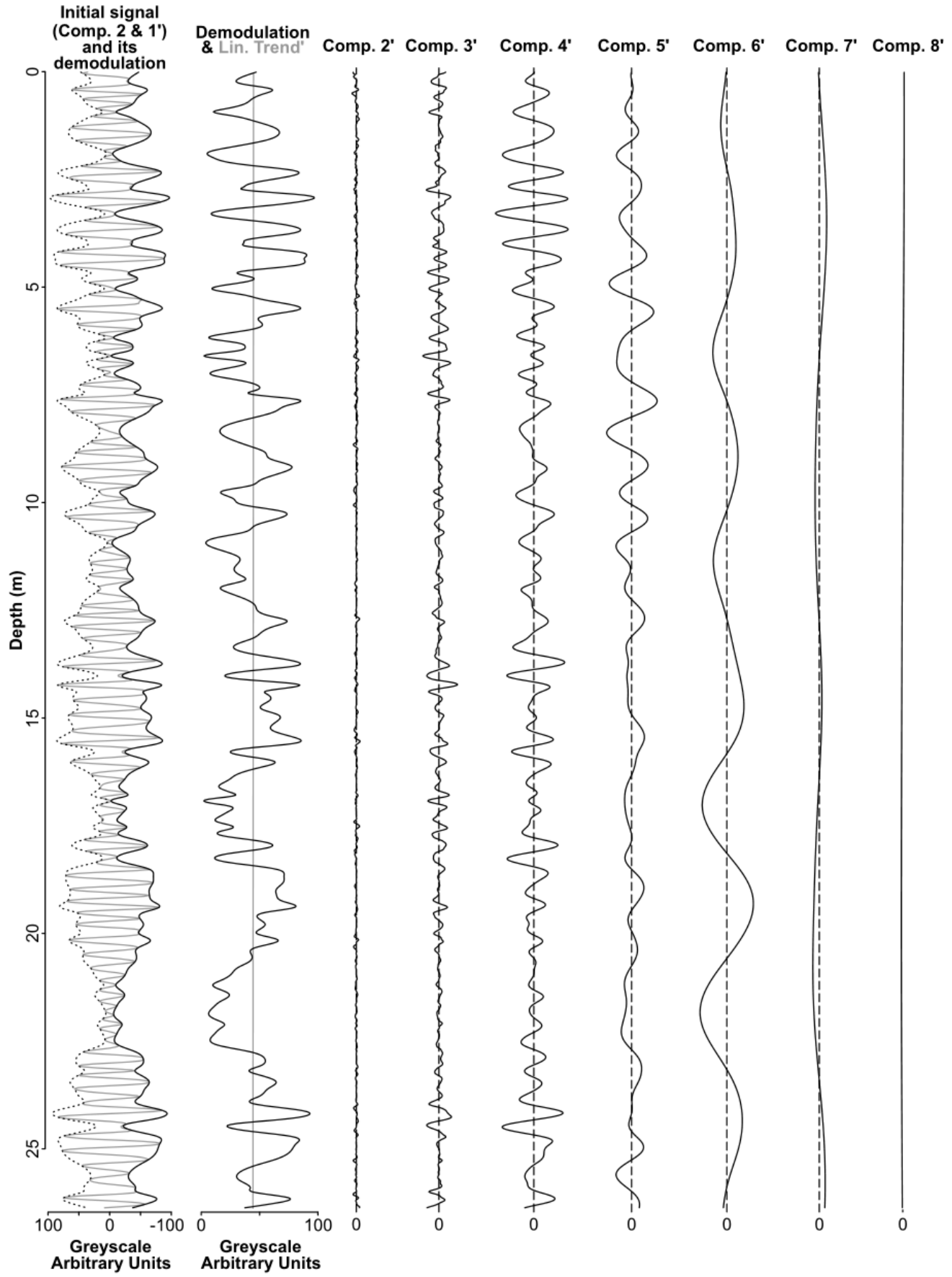
Initial signal
(Comp. 2 & 1')
and its
demodulation
Demodulation
& Lin. Trend'
Comp. 2'
Comp. 3'
Comp. 4'
Comp. 5'
Comp. 6'
Comp. 7'
Comp. 8'
Depth (m)
0
5
10
15
20
25
100
0
-100
0
100
Greyscale
Arbitrary Units
Greyscale
Arbitrary Units
0
0
0
0
0
0
0
0

Figure SF5

Figure SF5: EEMD decomposition of the amplitude demodulation of comp. 2 of the CIP1 signal decomposition (one isolated realisation, see Fig. SF4). The intensity scale is constant. Comp. 2, which is being demodulated, is attributed to the expression of climatic precession (ca. 23 kyr period), therefore the comp. 5', 6', 7' and 8 'are attributed to modulators of climatic precession, namely short and long eccentricity (ca. 125 and 405 kyr), and the g_1 - g_5 component (ca. 1000 kyr). The other components are discussed in the text.

The decomposition on the raw signal (Fig. SF4) extracts 5 components that can be attributed to astronomical cycles, at 23, 125, 405, 1000 and 2400 kyr periods in the comp. 2, 4, 5, 6 and 7 respectively (Figure SF8). These components correspond to climatic precession for comp. 2, and to amplitude modulators of climatic precession; short eccentricity for comp. 4, long eccentricity for comp. 5, the 1000 kyr g_1 - g_5 cycle for comp. 6 and the 2400 kyr $g_4 - g_3$ cycle for comp. 7 (e.g. Olsen and Kent 1999; Hinnov 2000; Laskar et al. 2011). The presence of amplitude modulators in the decomposition of the raw signal is due to a form of partial rectification. Partial rectification happens due to asymmetry in signals, which pours some of the cyclicity present in the amplitude modulation into the raw signal (see section 5.3.1 in Weedon 2003). The effect of partial rectification is evident in the CIP1 signal: Figure SF3B shows that the left side of the signal (at high arbitrary unit values) is smoother than the right side of the signal (at low arbitrary unit values). The loss of symmetry is a result of the simulated threshold mechanism that was introduced in the making the CIP1 case study (see section 9, and Sinnesael et al. 2019). The consequence of partial rectification is that amplitude modulation affects the mean of the raw signal (see Fig. SF3B), and can therefore be extracted as a component in the raw signal (section 5.3.1 in Weedon 2003). The amplitude modulation of climatic precession remains clearly visible in the raw signal decomposition, as shown in Figure SF8B (and Fig. SF4) where comp. 2 displays strong amplitude modulation. The high maximum amplitude values of comp. 2 are coherent with the prevalence of climatic precession, similarly to what is observed in the insolation solution periodogram (Fig. 17).

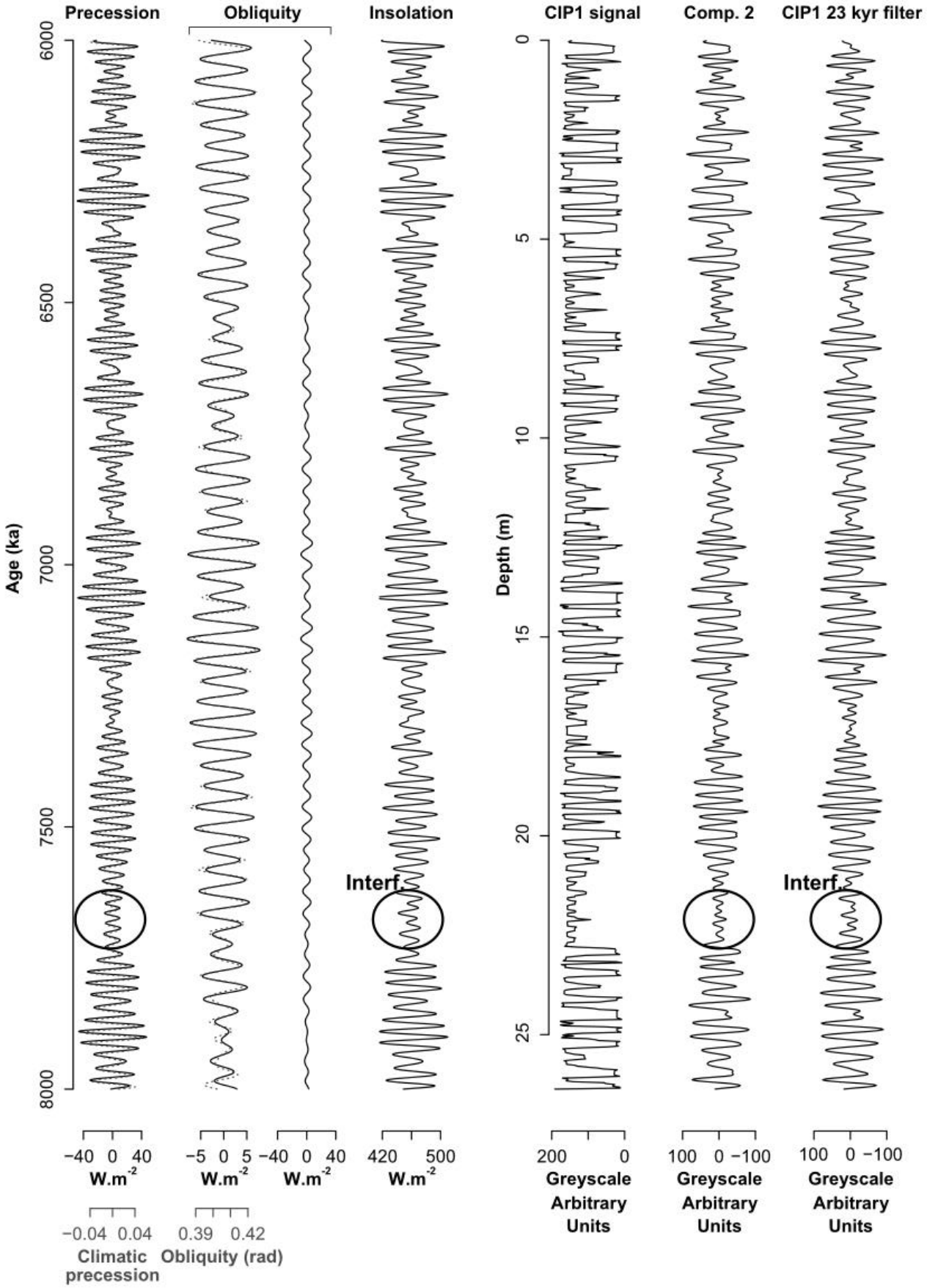
Precession
Obliquity
Insolation
CIP1 signal
Comp. 2
CIP1 23 kyr filter
Age (ka)
6000
6500
7000
7500
8000
Depth (m)
0
5
10
15
20
25
Interf.
Interf.
−40 0 40
W.m-2
−5 0 5
W.m-2
−40 0 40
W.m-2
420 500
W.m-2
200 0
Greyscale Arbitrary Units
100 0 −100
Greyscale Arbitrary Units
100 0 −100
Greyscale Arbitrary Units
−0.04 0.04
Climatic precession
0.39 0.42
Obliquity (rad)

Figure SF6

Figure SF6 : Comparison of climatic precession, either filtered from the 21 July insolation of Laskar et al. (2004) at 55°N between 8000 and 6000 ka (continuous black line) or directly obtained from the Laskar et al. (2004) model (dashed grey line), obliquity (same symbology as climatic precession, the right panel has similar scaling than climatic precession and insolation), the insolation curve itself, the CIP1 signal, comp. 2 and the CIP1 23 kyr filter. The interference pattern brought by obliquity is best expressed where the expression of climatic precession is weak (Interf. mention).

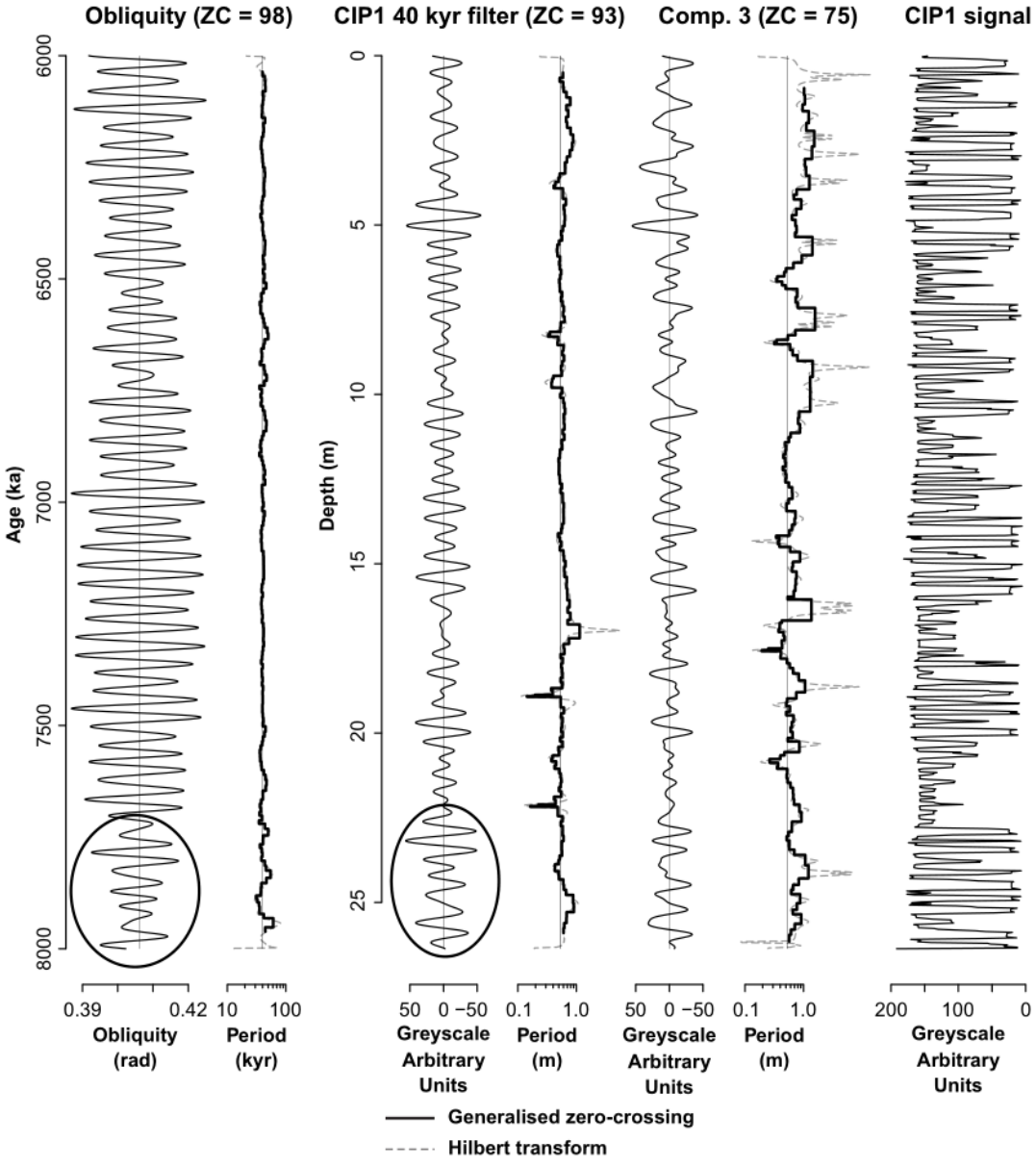

Figure SF7: Comparison of the expression and instantaneous frequencies of obliquity directly obtained from the Laskar et al. (2004) model, of a Taner filter of the CIP1 signal centred on the 40 kyr cycle, and of comp. 3. Some amplitude modulation is correctly extracted by the filter (circled parts) in parts of the signal where the climatic precession amplitude is not strongly modulated. Instantaneous frequency is generally correct for the filter. The decomposition fails to meaningfully extract obliquity. ZC stands for the number of zero-crossings. The fine straight line stands for the mean, or for 0, in the signal components, and for the expected obliquity periods (40 kyr or 40 kyr * 75.81 m.kyr^{-1}) in the instantaneous frequency graphs.

An increase of the sedimentation rate can be observed in places where the greyscale variations are stronger (Fig. SF9). This is coherent with the way the stratigraphic depth was computed: the thickness of darker beds was made to higher relative to the lighter beds, and these darker beds are concentrated in places where the variations of amplitude are strongest (Fig. SF3 and SF4).

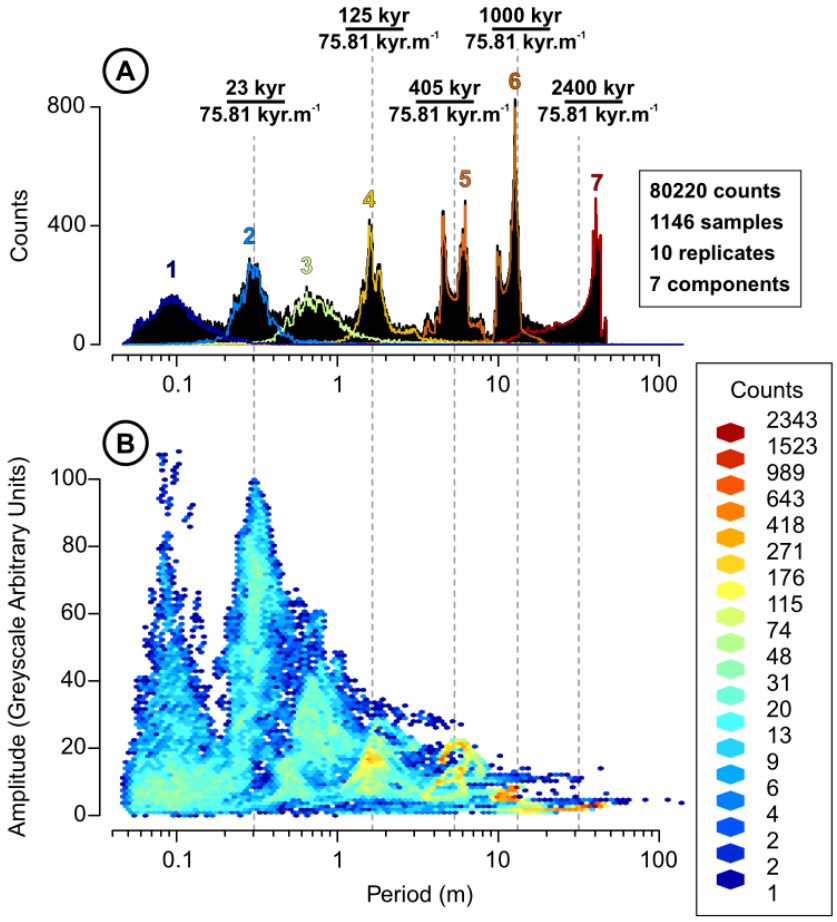

Figure SF8: (A) Period distribution and (B) spectral population of the components of CIP1 decomposition (ensemble of 10 replicate decompositions with identical parameters but with different white noise realisations; see also Fig. SF4). The doted lines stand for the expected periods of climatic precession (ca. 23 kyr), and of climatic precession modulators: short-eccentricity (ca. 125 kyr), long eccentricity (405 kyr), the g_1 - g_5 cycle (ca. 1000 kyr) and the g_4 – g_3 cycle (ca. 2400 kyr) (e.g. Olsen and Kent 1999; Hinnov 2000; Laskar et al. 2011).

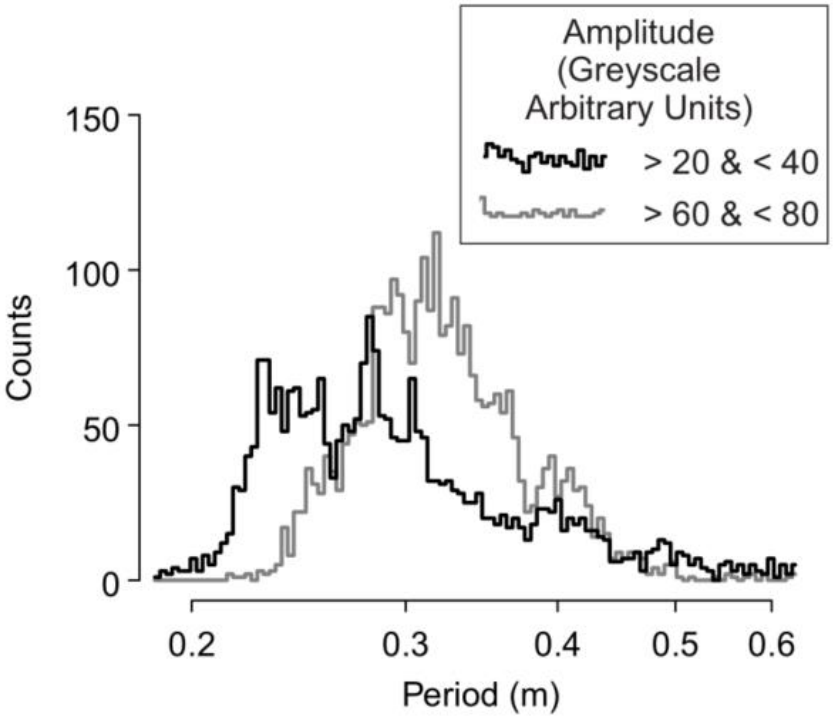

Figure SF9: (A) Period distribution of comp. 2 (ensemble of 10 replicate decompositions with identical parameters but with different white noise realisations): the distribution is divided between "low amplitude" (between 20 and 40 greyscale arbitrary units, shown has the black line) and "high amplitude" (between 60 and 80 greyscale arbitrary units; shown has the grey line). The period distribution shifts towards higher values in the "high amplitude" curve, which indicates that sedimentation rate is indeed higher when the amplitude is higher.

The frequency ratios of the component pairs 2-4, 2-5 and 2-6, corresponding to the couples of periods 23-125 kyr, 23-405 kyr and 23-1000 kyr (Fig. SF10 B, C and D respectively), are standing out even in the general ratio population plot (Fig. SF10A), by their high squared ratio power and their focalised frequency ratio distribution. Another frequency ratio value is highlighted in a similar fashion, with high squared ratio power and well concentrated distribution, around a value of 2 (at the centre of the grey rectangle in Fig. SF10A). This is interpreted to be due to the dyadic nature of modally meaningful decomposition methods (see section 4.3). No ratio containing the 2400 kyr cycle is clearly expressed, probably due to its small amplitude in comp. 7.

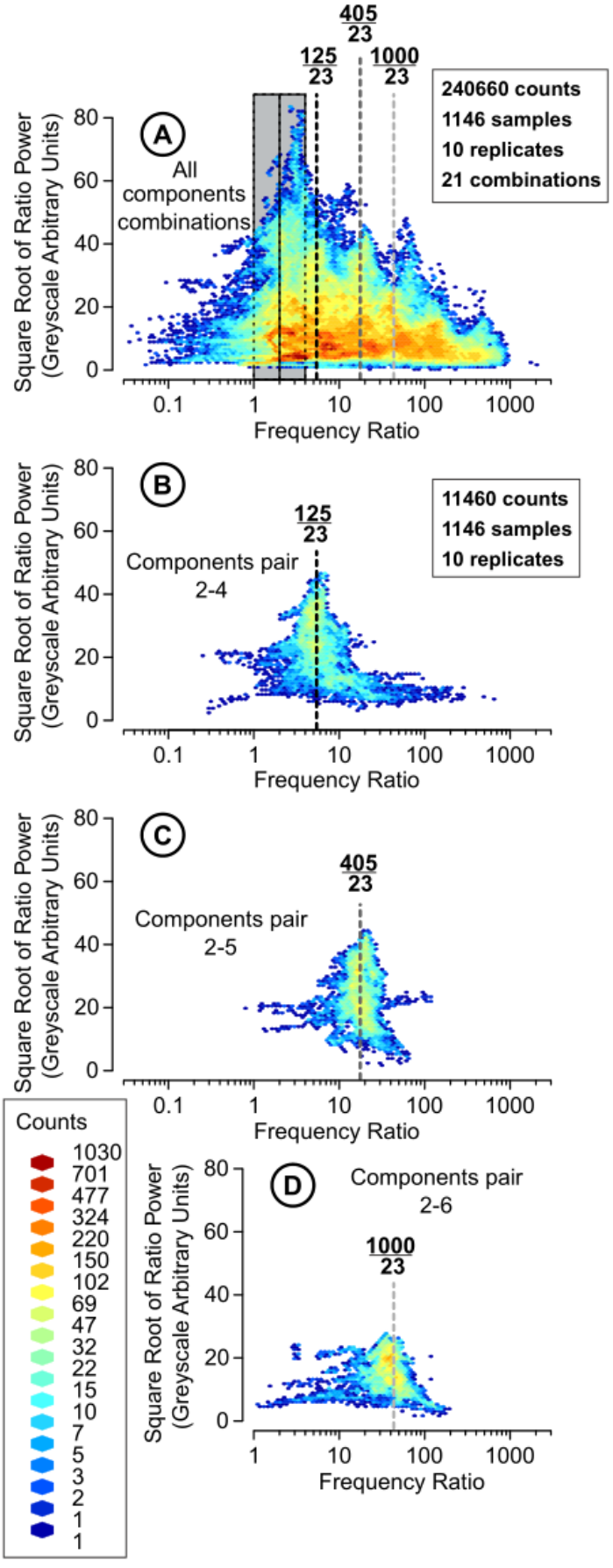
405/23
125/23
1000/23
240660 counts
1146 samples
10 replicates
21 combinations
A
All components combinations
Square Root of Ratio Power (Greyscale Arbitrary Units)
Frequency Ratio
B
11460 counts
1146 samples
10 replicates
Components pair 2-4
C
Components pair 2-5
D
Components pair 2-6
Counts
1030
701
477
324
220
150
102
69
47
32
22
15
10
7
5
3
2
1
1

Figure SF10

Figure SF10: (A) Ratio population for all pairs of components of the CIP1 decomposition, and (B, C and D) for selected components pairs interpreted as climatic precession/short-eccentricity, climatic precession/long-eccentricity and climatic precession/g_1 - g_5 (ensemble of 10 decompositions with identical parameters but with different white noise realisations). The dotted lines stand for some of the expected frequency ratios (see section 5.1, and Fig. 17). The grey rectangle delimits frequency ratios between 1 and 4, and is centred on a ratio of 2.

The decomposition on the amplitude demodulation of comp. 2 (Fig. SF5) extracts cycles at 125, 405 and 1000 kyr (Fig. SF11). The fact that the climatic precession modulators are clearly expressed confirms that climatic precession is well recorded in comp. 2. It should be noted that comp. 2, or 1', i.e. the one used to determine the demodulation (Fig. SF4 and SF5), is repeated 10 times in the distribution plots to have a similar behaviour. An artefact of such a practice is that there are 10 similar points each time, therefore the counts for that component are systematically superior to 10 in Figure SF11B. And the amplitude of comp. 2 (1') is higher than any other component in this decomposition, which makes sense as the other components are derived from its amplitude demodulation. Comp. 6', attributed to the 405 kyr cycle, is particularly regular and well-expressed (Fig. SF11). The good expression of the 405 kyr cycle echoes the behaviour observed in the periodogram of the demodulated insolation (Fig. 17B), where the 405 kyr long-eccentricity cycle has the highest spectral power.

The frequency ratios of the demodulation of comp. 2 are shown in Figure SF12, again based on the 23 kyr component, underlining the predominance of the 23– 125 kyr, 23 – 405 kyr and 23 – 1000 kyr pairs. The 23 – 405 kyr pair is particularly well expressed and regular.

The presence of the 2400 kyr cycle in the demodulation of comp. 2 is hinted in both raw frequencies and ratios of frequency (Figs. SF11 and SF12). However the cycle is of very low amplitude, and its phase does not match well with what is expected from the astronomical solution, as can be seen in Figure SF13. This stresses the necessity to visualise the cycles extracted and interpret them critically.

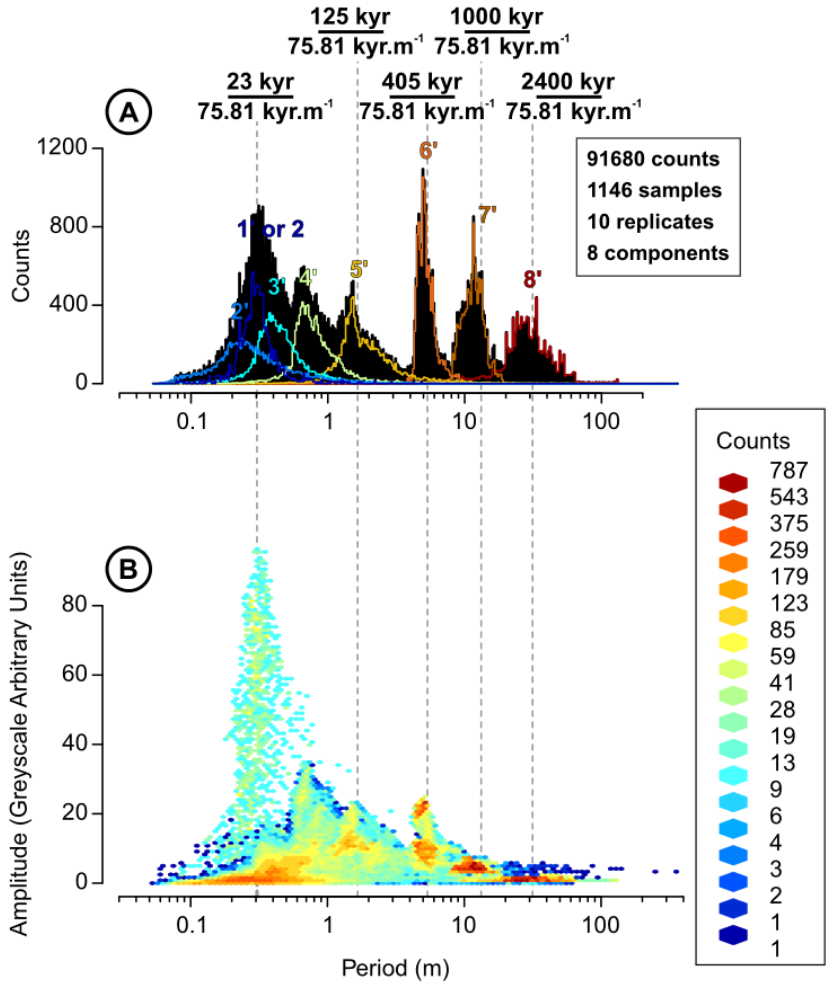

Figure SF11: (A) Period distribution and (B) spectral population of the components of the decomposition (ensemble of 10 decompositions with identical parameters but with different white noise realisations) of the amplitude demodulation of one realisation of comp. 2 of the CIP1 signal decompositions (see Fig. 19). The doted lines stand for the expected periods of climatic precession (ca. 23 kyr), and of climatic precession modulators: short-eccentricity (ca. 125 kyr), long eccentricity (405 kyr), the g_1 - g_5 cycle (ca. 1000 kyr) and the g_4 – g_3 cycle (ca. 2400 kyr). Comp. 1' stands for the comp. 2 of the CIP1. Note that comp. 1' has sensibly more amplitude than the others, being the original component at the source of the demodulation. Further note that because comp. 1' is an isolated realisation repeated 10 times, there are no surface with less than 10 points for that specific component.

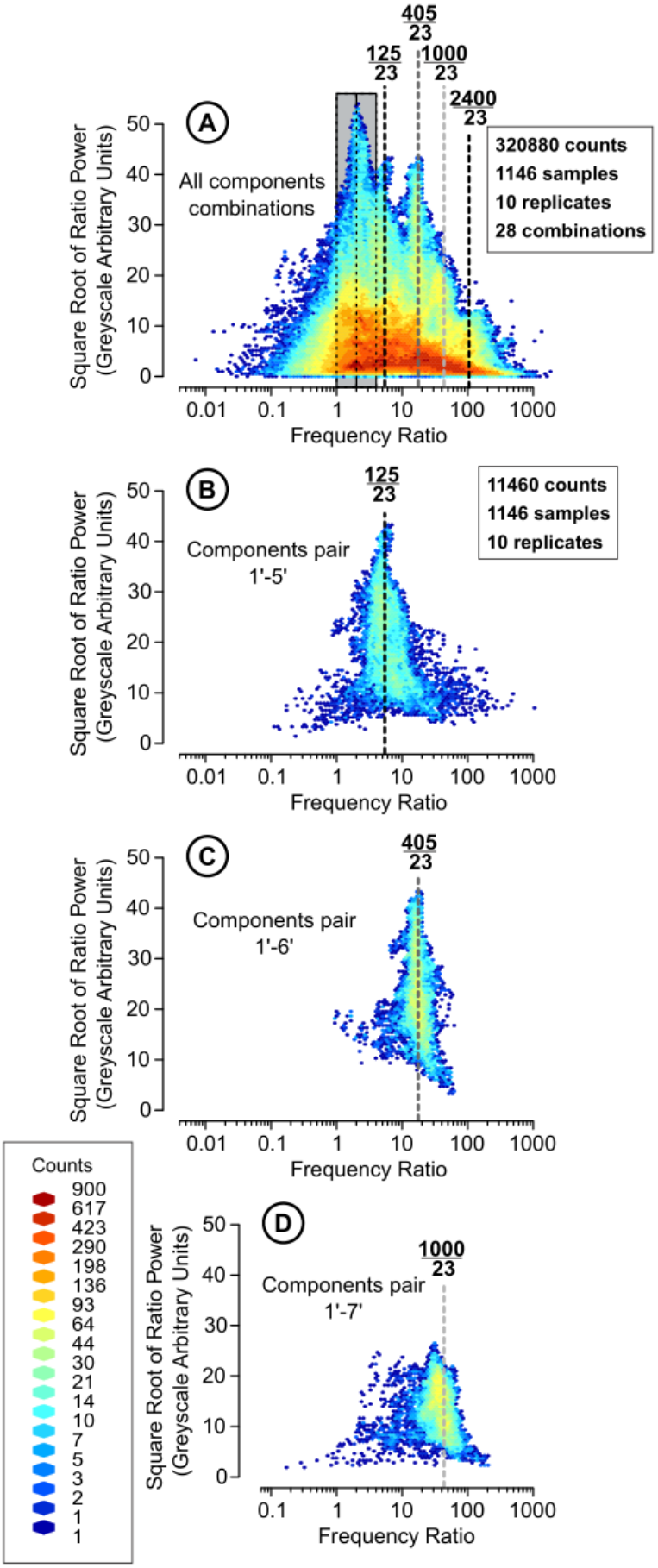
A
405
23
125
23
1000
23
2400
23
320880 counts
1146 samples
10 replicates
28 combinations
All components
combinations
Square Root of Ratio Power
(Greyscale Arbitrary Units)
Frequency Ratio
B
125
23
11460 counts
1146 samples
10 replicates
Components pair
1'-5'
C
405
23
Components pair
1'-6'
D
1000
23
Components pair
1'-7'
Counts
900
617
423
290
198
136
93
64
44
30
21
14
10
7
5
3
2
1
1

Figure SF12

Figure SF12: (A) Ratio population for all pairs of components of the amplitude demodulation of one realisation of comp. 2 of the CIP1 signal decompositions (see Fig. 19), and (B, C and D) for selected components pairs interpreted as climatic precession/short-eccentricity, climatic precession/long-eccentricity and climatic precession/g_1 - g_5 (ensemble of 10 decompositions with identical parameters but with different white noise realisations). The dotted lines stand for the expected frequency ratios. The grey rectangle delimits frequency ratios between 1 and 4, and is centred on a ratio of 2.

The components attributed to the 125, 405, 1000 and 2400 kyr cycles, extracted from the raw signal (respectively the comp. 4, 5, 6 and 7) and from the amplitude of comp. 2 or 1' (namely the comp. 5', 6', 7' and 8') are plotted in Figure SF13. The components extracted from the raw signal are comparable to the components extracted from the demodulation of component 2 or 1', except for the 2400 kyr cycle. These components are compared to filters of the direct demodulation of the insolation solution (Fig. SF13). The extraction of the 405 kyr and 1000 kyr cycles fit well, however the extraction of the short-eccentricity by the decomposition is problematic where the short eccentricity has low amplitude. The amplitude modulation of short eccentricity can nevertheless be identified in comp. 4 and 5'. The 2400 kyr cycle is clearly identified from the raw signal in comp. 7, but is more problematic in the decomposition coming from the demodulation; i.e. comp. 8'. However, what is shown in Fig. SF13 is only one of the 10 replicates of decomposition obtained: the instantaneous frequency of the 10 replicates in the spectral population plot (Fig.SF11B) is well centred on a 1/2400 kyr frequency. The deviation could originate from the very low amplitude of the cycle, and the fact that it is the remainder of the decomposition, having a period greater than the length of the signal; in other words a cyclically-connoted residual.

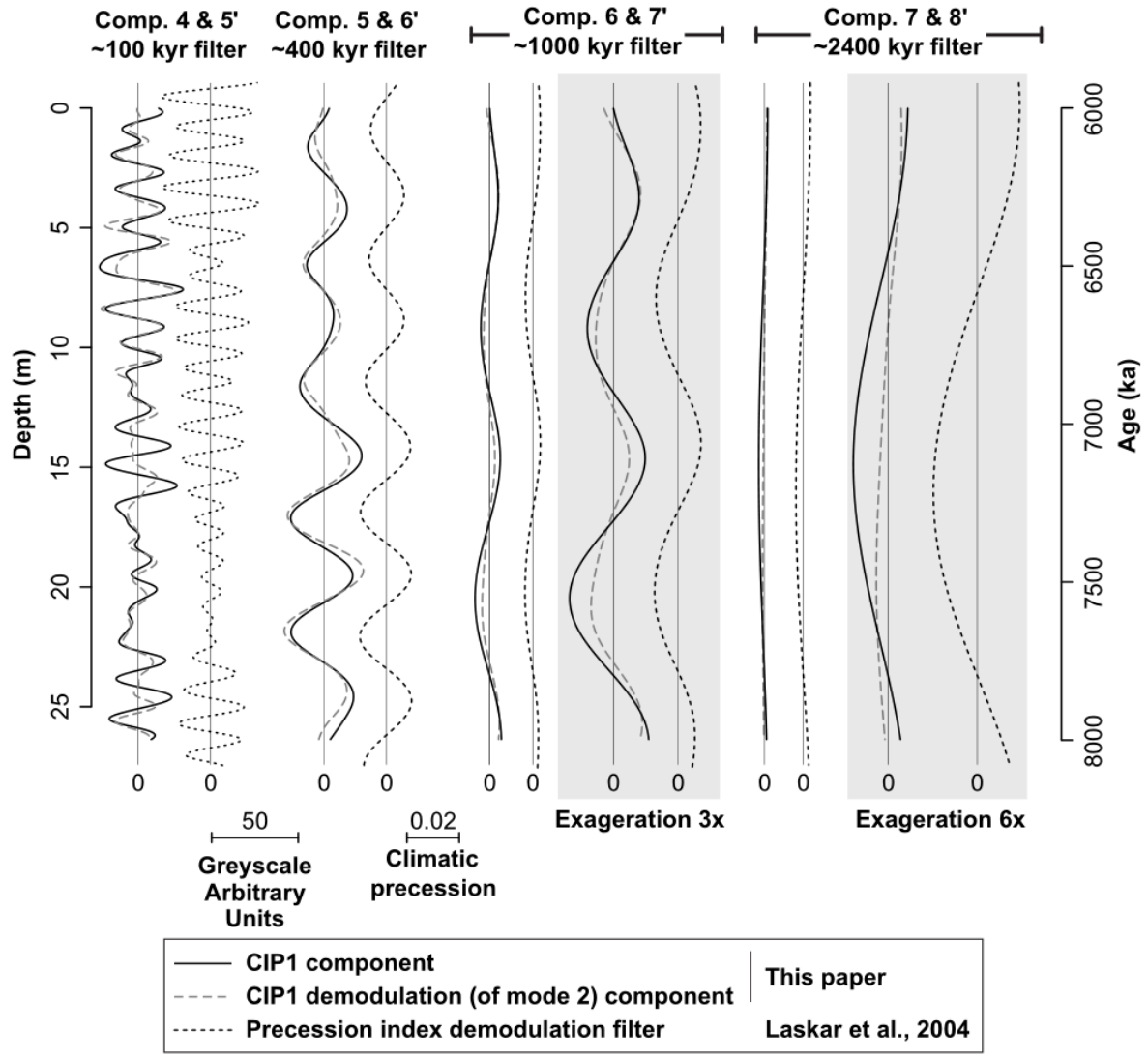

Figure SF13: Comparison between the supposed 125, 405, 1000 and 2400 kyr cycles obtained from (I) decomposition of the raw signal (comp. 4, 5, 6 and 7) and (II) from the demodulation of one realisation of comp. 2 (1') of the CIP1 signal decomposition (comp. 5', 6', 7' and 8') to (III) the climatic precession index demodulation (Laskar et al., 2004). The good agreement between the signal and the demodulation comes from amplitude modulation being leaked into the record by partial rectification (see section 5.3.1 in Weedon 2003). The comparison of the cycles obtained from the signal to the ones obtained from the demodulation of the climatic precession index show equally good agreement.

The influence of obliquity is not readily recognised in the decompositions of CIP1 (Fig. SF6 & SF7). We attempted to identify the expression of obliquity in the CIP1 23 kyr filter (Fig.SF6) and CIP1 40 kyr (Fig. SF7) filters. Obliquity plays only a minor role in the insolation signal at 55°N, which is illustrated by low spectral power in the insolation periodogram (Fig. 17A). The expression of obliquity is highly cross-cancelled with the expression of climatic precession (Fig. SF6). Indeed, filters of the climatic precession and obliquity of the insolation signal, when treated like a decomposition, account for respectively 94% and 18% of the absolute intensity of insolation, leaving a remainder making up to 6% of that absolute intensity. There is therefore 118% of absolute intensity of insolation in that specific decomposition (parsimony = 1.18). When adding the obliquity and climatic precession

filters of the insolation solution back together, they account for 97% of the absolute intensity of insolation, meaning that the equivalent of 15% of the absolute intensity of insolation, i.e. more than 80% of the absolute intensity in the obliquity filter, gets cross-cancelled in the process. The effect of mixing climatic precession and obliquity is therefore in all probability to create interference patterns. This can be best observed in places where climatic precession is weakly expressed, in which case the interference pattern can be identified in the CIP1 23 kyr filter (see Interf. mention in Fig. SF6). In the CIP1 40 kyr filter (Fig. SF7), the amplitude modulation of the expression of obliquity on insolation can be recognised in intervals where the expression of climatic precession is only weakly modulated (e.g. in maxima of amplitude modulation, see circled parts in Fig. SF7). However, the impact of the amplitude modulation on the expression of climatic precession dominates in the amplitude modulation of the CIP1 40 kyr filter, making it difficult to cleanly extract the amplitude modulators of the expression of obliquity on the insolation. The instantaneous frequency of the CIP1 40 kyr filter is generally coherent with the predicted frequency, only missing a few zero-crossings (meaning that some obliquity peaks are lost).

The "extricate" decomposition fails to recover climatic precession with easily identifiable obliquity interference patterns (Fig. SF6), or to extract a reliable signal for obliquity (Fig. SF7). The comp. 3 shifts to lower instantaneous frequencies, and the signal extracted is of generally bad quality (Fig. SF7). It would be tempting to attribute this to another cycle of longer period, but we dismiss this interpretation due to the fact that no such cycle is present in the insolation solution (Fig 17).

23 kyr	**125 kyr**	**405 kyr**	**1000 kyr**
Comp. 2	Comp. 4	Comp. 5	Comp. 6
1.13	1.23	1.08	1.08
Comp. 1' (2)	Comp. 5'	Comp. 6'	Comp. 7'
1.12	1.29	1.07	1.15

Table ST1: GZC departure of components attributed to specific astronomical cycles, identified by their main period (see Fig. SF4 and SF5). The lowest GZC departure is found for long eccentricity extraction (405 kyr); the 1.08 GZC departure gives an 8% error on frequency, i.e. an average error interval from incorrect instantaneous frequency computation between 375 and 437 kyr considering a mean period of 405 kyr.

Comp. 1	Comp. 3
1.44	1.25

Comp. 2'	Comp. 3'	Comp. 4'
1.59	1.27	1.20

Table ST2: GZC departure of components that are not representative of astronomical cycles. The highest GZC departure (1.59) is found in comp 2', which means that incorrect instantaneous frequency computation in that component gives an average 59% error on frequency.

The integrity of our two decompositions (on the raw signal and on the demodulation of component 2) is under 10^{-14} arbitrary units, which falls well into acceptable limits for our intensity values. The parsimony of both decompositions is under 1.65. The GZC departure of each component (except the residuals comp. 7 and 8'), averaged for the 10 replicates of each components, is presented in Tables ST1 and ST2. The lowest GZC departures occur for the components attributed to the 23, 405 and 1000 kyr cycles. The low GZC departure values of the 23 and 405 kyr are good indicators that these components are so well expressed in the signal that they can be extracted in a cleaner fashion than any other cycle. Indeed, these components are the best expressed in the record in terms of amplitude (see Fig. SF8 for the 23 kyr component, and Fig. SF11 for the 405 kyr component), and their frequency ratio distribution is fairly well concentrated (Figs. SF10C and SF12C). The highest GZC departure values are found in the first components of the decompositions (1 and 2'). This could be due to the fact that these are taking in the steepest variations of frequencies, some of them having their minima and maxima follow each other without necessarily having samples in between. The two residuals, comp. 7 and 8', have an insufficient number of extrema to compute the frequency via the GZC methodology. To discuss the accuracy of the instantaneous frequency determination, we can use the symmetry metric. For comp. 7, it is encompassed between 0.7 and 0.9 for its 10 replicates, whereas for comp. 8' it ranges from 0.5 to 1, i.e. the entire range of possibilities. This again underlies that comp 8', the cyclically-connoted residual with a very low amplitude, can be extracted very differently by different realisations of the decomposition. On the opposite the values are relatively stable for comp. 7, and are not reaching 1 entirely (i.e. without any zero-crossing), which is a good indicator that it might represent a meaningful cycle (the 2400 kyr one), and that the frequency estimation might provide useful information.

The expression of climatic precession and of its amplitude modulators is found in comp. 2 (1'), comp. 4 to 7, and comp 5' to 8'. This raises the question of what is contained in the other components (comp. 1 & 3, comp 2' & 3', and the linear trends). As described earlier, comp. 3 can be understood as a strongly distorted expression of obliquity, for which the instantaneous frequency locally shifts to lower frequencies (Fig. SF7). The first component of the raw signal decomposition, comp. 1, represents the highest frequencies in that decomposition. It punctually presents high amplitude variations (Fig. SF8B), but has a large frequency distribution (Fig. SF8A). Upon close visual inspection (in Fig. SF4), most of the comp. 1 high amplitude peaks correspond to the steep edge of high amplitude fluctuations in the CIP1 signal. This could indicate that it is an effect of the sharply angular nature of the signal that appeared when converting the insolation signal into given lithological classes. Comp. 1 also takes amplitude from single-sample pulses. This is an effect inherent to the discrete nature of the data, and as

comp.1 represents the highest frequency, it is this component that will include such single-sample peaks. In the decomposition of the demodulation of comp. 2 (1'), comp. 2' and 3' have small amplitudes (Fig. SF11B), frequencies similar or below to comp. 2 (1') (Fig. SF11A), and are interpreted to be due to imperfections in the normalisation and decomposition procedures. Comp. 4', however, has strong amplitude, and has periods of more than two times the periods of comp. 2 (1') (SF11). We interpret these fluctuations to stem from any amplitude differences between successive peaks in comp. 2, which would be followed by the demodulation. Finally, the linear trends do not contain any patterns; in fact with the CIP1 signal they could easily be replaced by the mean of the initial signals.

10.2 ODP 926 Magnetic susceptibility signal

The magnetic susceptibility signal of ODP 926 is very similar to its greyscale counterpart; we therefore treat it and interpret it similarly, but with a few nuances. We decompose the magnetic susceptibility signal in 10 components using "extricate" (Figs. SF14 and SF15): MSC (for Magnetic Susceptibility Component) 1 through 9, plus a nonlinear trend (the addition of a 10^{th} component and the linear trend). Unlike the greyscale signal, we make two replicates of the signal, to compensate, in the plots of instantaneous parameters, for the smaller number of points (2070) than the greyscale signal (7189). We perform the decomposition in the stratigraphic domain after interpolation to regularly spaced samples using the stratigraphic quanta as resampling interval. This is to reduce mode mixing between intervals having different sampling rates (compare the intervals around 5250 ka and around 7500 ka to the other ones; Figs. SF14 and SF15). The interpolated points are removed after decomposition to only keep the original data points for further data processing. Each replicate is obtained from averaging 100 realisations, having different uniform white noise realisations, contained within ± 25 magnetic susceptibility sensor values, added to them. For comparison, the signal values are ranging between 0 and 30 magnetic susceptibility sensor values. The sifting is not iterated. These parameters where chosen so that MSC3 agrees well with the p-0.5t tuning target (Figs. SF14 and SF15). The rational for this parametrisation is identical than the treatment of the gresycale signal (section 5.2). MSC3 is demodulated using the scheme of Huang et al. (2009). The amplitude demodulation of MSC3 is decomposed using "extricate" with 2 siftings, on 2 replicates, each made of 100 realisations of white-noise added realisations (limited to ± 5 magnetic susceptibility sensor values). Other than the above-mentioned parametrisation, the data analysis methodology applied on the magnetic susceptibility signal is identical to the one performed on the greyscale one. The R script for the time-series analysis performed on the ODP 926 magnetic susceptibility signal is available as supplementary material SC3.

Similarly to GSC3 in the greyscale signal, MSC3 is attributed to climatic precession, with a possible influence of obliquity; it is well centred on 20 kyr (Fig. SF16), and follows the tuning target closely (Fig. SF14 and SF15). MSC4 is centred roughly on 40 kyr (Fig. SF16), therefore it could be representative of obliquity. However, it does overlap with MSC3 in tuned instantaneous frequency (Fig. SF16D), so we expect some interference between climatic precession and obliquity. MSC 5, 6, 7 and 8 have mean periods comparable to the eccentricity cycles of 100, 400, 1000 and 2400 kyr respectively (Fig SF16). The comparison to Laskar et al.'s solution shows that MSC6 fits the 400 kyr cycle only between 9000 and 7000 ka (Fig. SF17). This is similar to GSC6 in the greyscale signal. The magnetic susceptibility is, contrary to the greyscale one, not presenting a step-like increase of values around 7950 ka (see Fig. 16). Without this disturbance, the 1000 kyr cycle is actually hinted in MSC7 (Fig. SF17). MSC 5 and 8 on the other hand are not well in phase with the 100 kyr and 2400 kyr cycle solutions respectively (Fig. SF17), despite showing similar mean periods (Fig SF16).

MSC 1 and 2 can be interpreted as natural or instrumental white noise. MSC1 shows slightly higher periods than its equivalent in the greyscale signal's GSC1, which can be explained by the higher sampling rate in the latter. MSC9 displays very low amplitude variations (Fig. SF16), making it hard to interpret in any meaningful way.

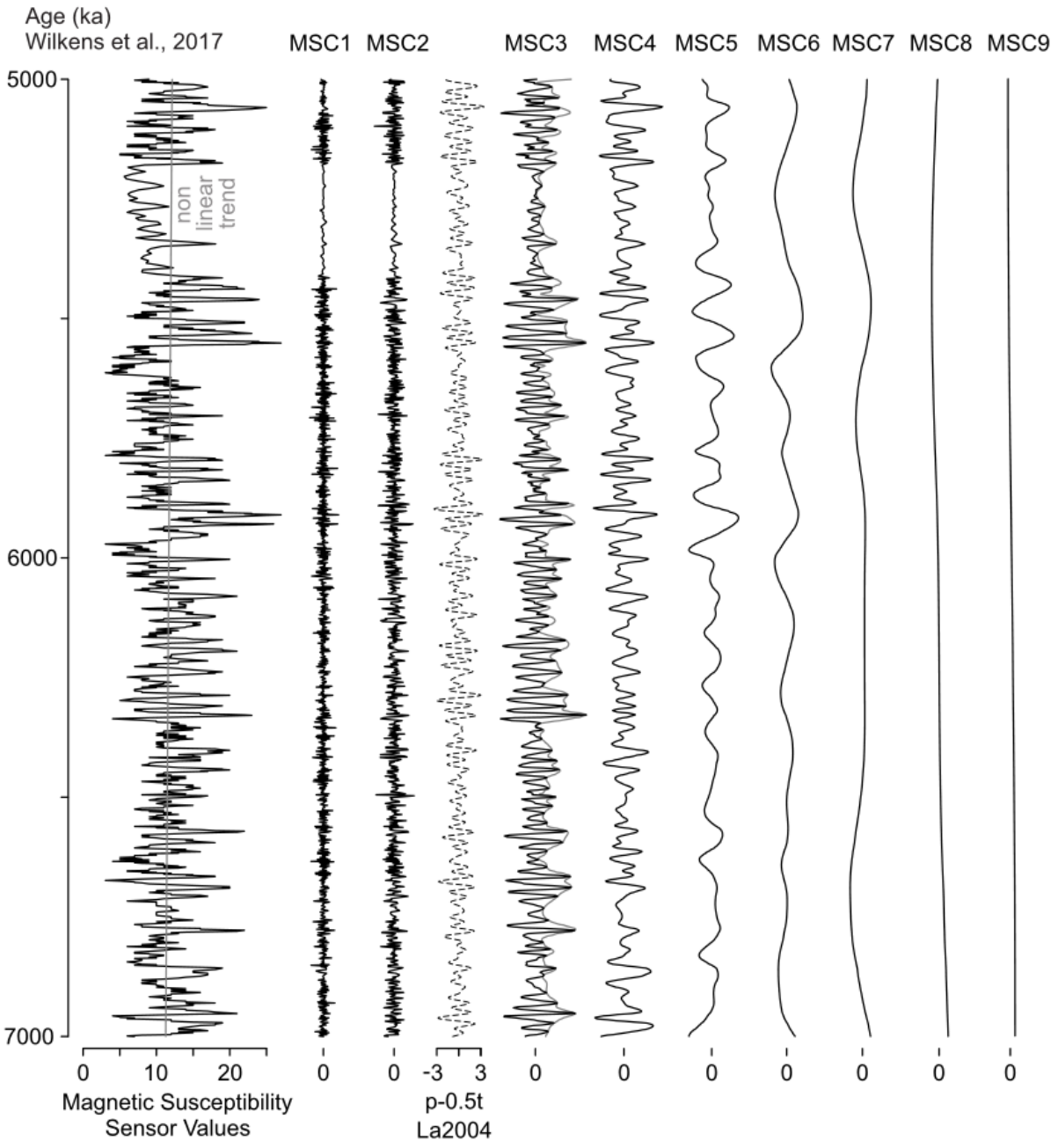

Figure SF14: EEMD decomposition the magnetic susceptibility signal of ODP 926 (upper part, between 7000 and 5000 ka). The intensity scale is identical for each component (MSC for Magnetic Susceptibility Component). The linear trend (grey line through the signal) is part of the decomposition. The decomposition was performed in the stratigraphic domain, and its output is here plotted in the time domain using the tuning interpretation of Wilkens et al. (2017). The tuning target used by Zeeden et al. (2013), based on the climatic precession (p) and tilt (t) modelled by Laskar et al. (2004), is shown for reference to the left of MSC3. The amplitude demodulation of MSC3 is shown in grey against MSC3. The amplitude modulation of MSC3 can be seen to parallel that of the tuning target (p-0.5t). The other components are discussed in the text.

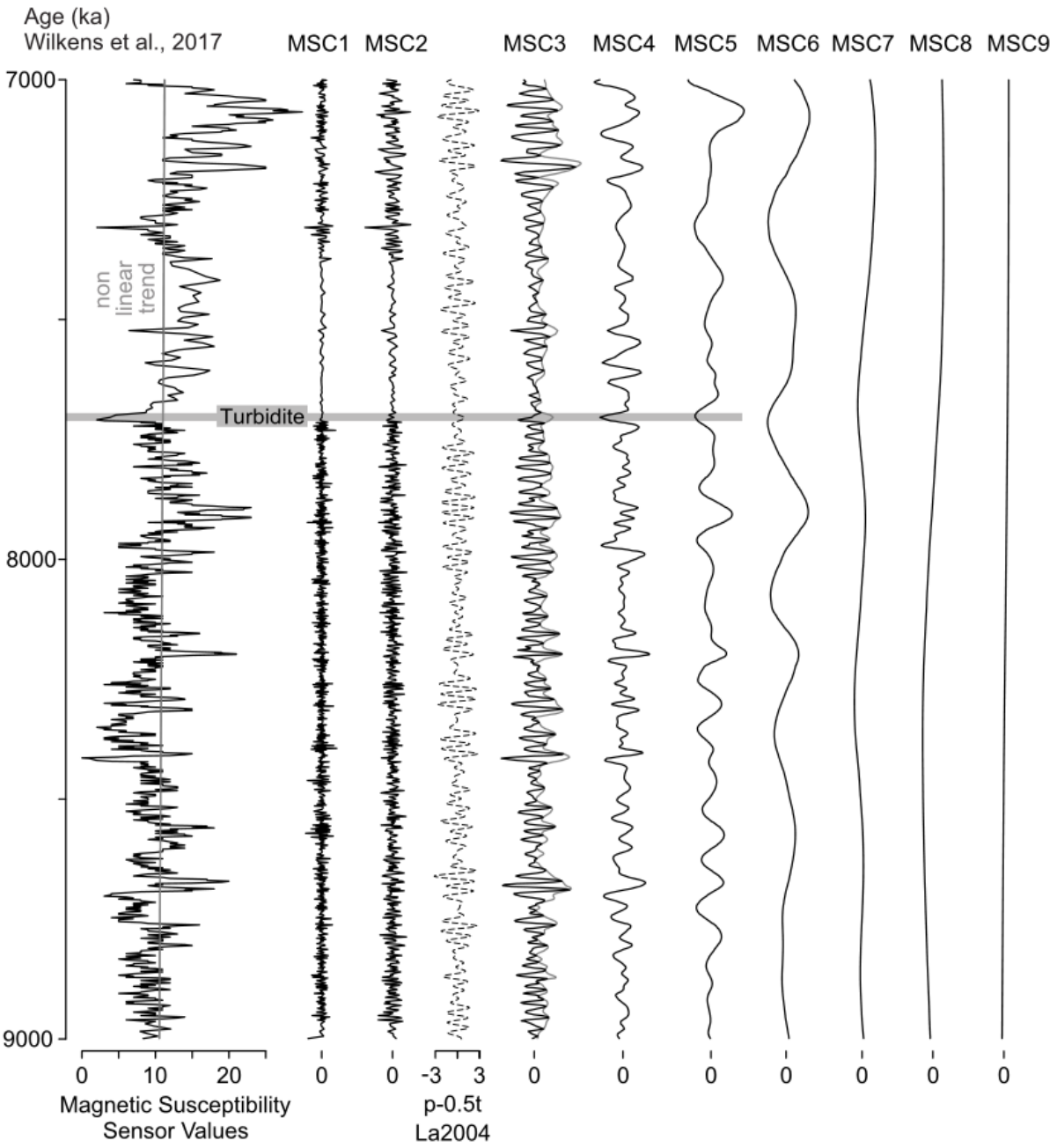

Figure SF15: EEMD decomposition the magnetic susceptibility signal of ODP 926 (lower part, between 9000 and 7000 ka). The expression of the 405 kyr long eccentricity cycle is quite noticeable in GSC6. The turbidite is found in the decomposition as wiggles in MSC 3, 4 and 5. See caption of Figure SF11 for further information.

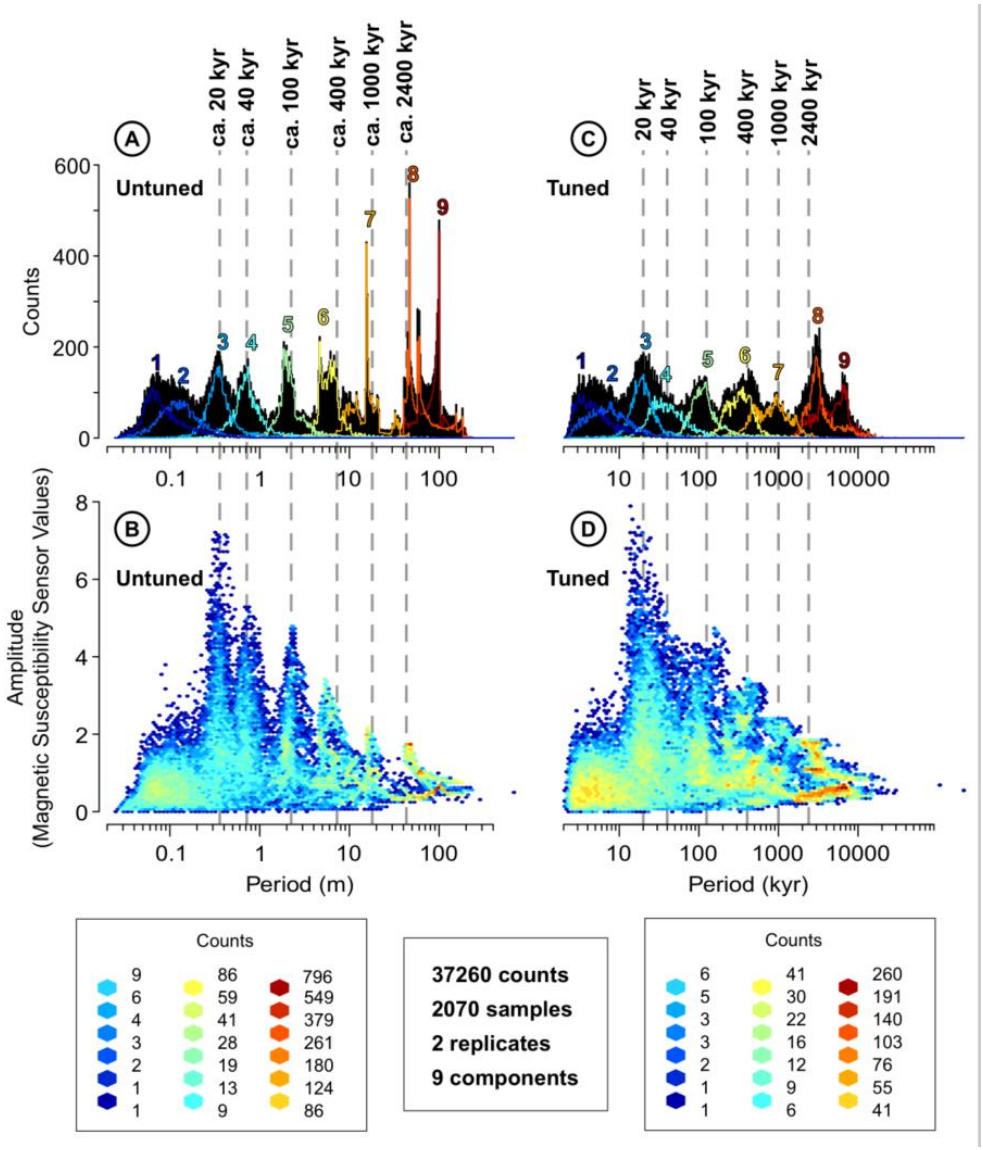

Figure SF16: comparison of the behaviour of instantaneous frequency in the stratigraphic domain (untuned) and in the time domain (tuned following the interpretation of Wilkens et al., 2017). (A) Period distribution, (B) spectral population of the untuned decomposition of the magnetic susceptibility signal of ODP 926, (C and D) against their respective equivalent for the time domain decomposition. The tuning was performed after the decomposition (i.e. the only difference is the y axis).

We compare our amplitude demodulation to the one performed by Shackleton and Crowhurst (1997); both extract equally well the 400 kyr cycle and the 1000 kyr cycles, but the 2400 kyr cycle is incorrect in both methodologies (Fig. SF17). The 100 kyr astronomical cycles are well identified by Shackleton and Crowhurst (1997), complete with their amplitude modulation, while in our methodology some cycles are extracted, but most of them are lost (Fig. SF17). The frequency ratios of the raw decomposition, and of the demodulation of MSC3, both show high squared ratio power and are well centred on the expected values (Figs. SF18 and SF19).

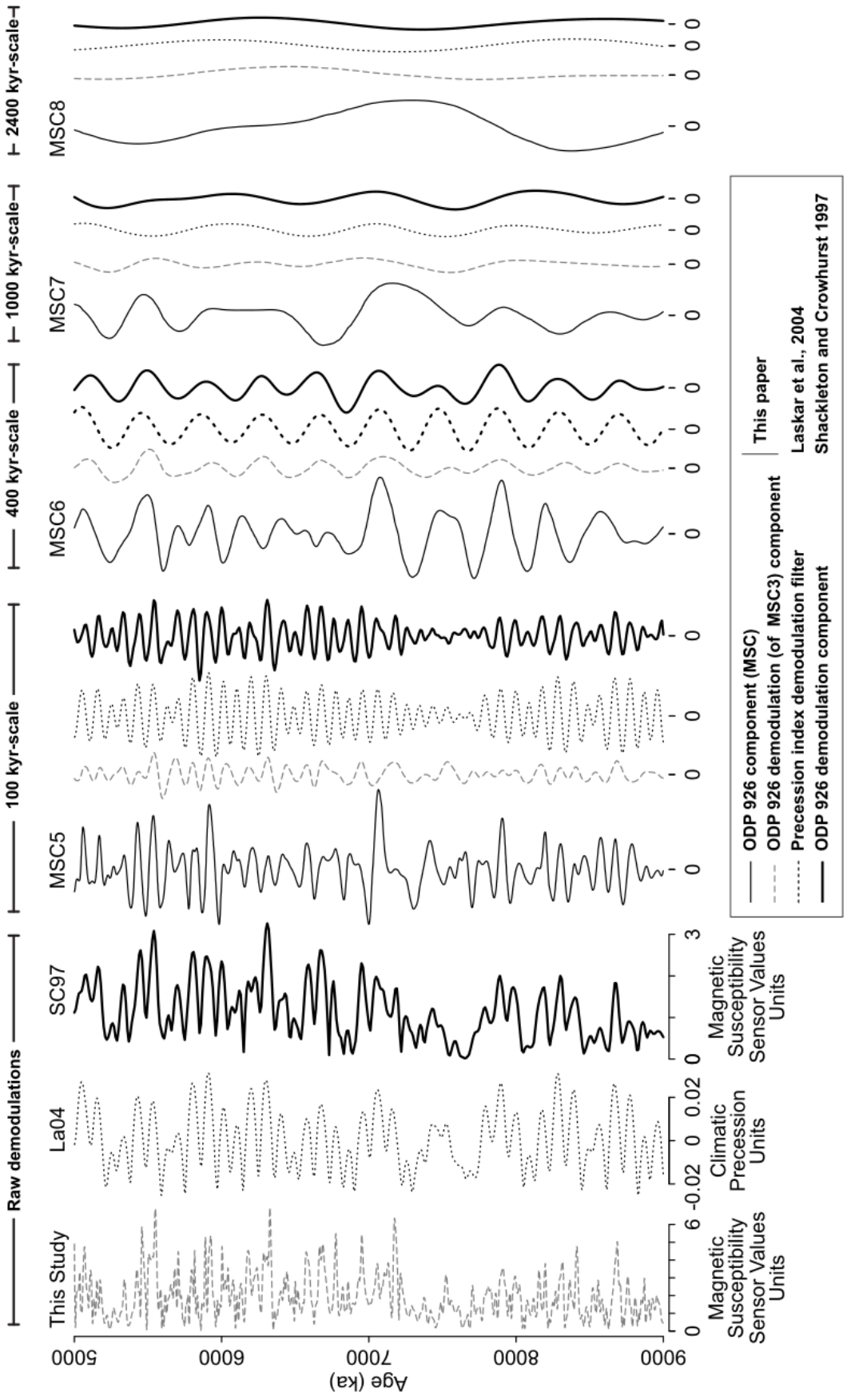
Raw demodulations
100 kyr-scale
400 kyr-scale
1000 kyr-scale
2400 kyr-scale
This Study
La04
SC97
MSC5
MSC6
MSC7
MSC8
Magnetic Susceptibility Sensor Values Units
Climatic Precession Units
Age (ka)
5000
6000
7000
8000
9000
ODP 926 component (MSC)
ODP 926 demodulation (of MSC3) component
Precession index demodulation filter
ODP 926 demodulation component
This paper
Laskar et al., 2004
Shackleton and Crowhurst 1997

Figure SF17

Figure SF17: Comparison of demodulations of the ODP 926 magnetic susceptibility signal. The raw demodulations from this study and from Shackleton & Crowhurst (1997) are decomposed, the raw demodulation of the climatic precession (Laskar et al., 2004) is filtered. They are and compared in groups, respectively representing of the ca. 100, 405, 1000 and 2400 kyr-scale cycles. The corresponding MSC are provided for comparison. The intensity scales are similar to the raw demodulations (in arbitrary units the decomposition and demodulations of the ODP 926 magnetic susceptibility signal performed in this paper, in –possibly different- arbitrary units for the demodulation performed by Shackleton & Crowhurst, 1997, and in climatic precession values for the Laskar et al. solution).

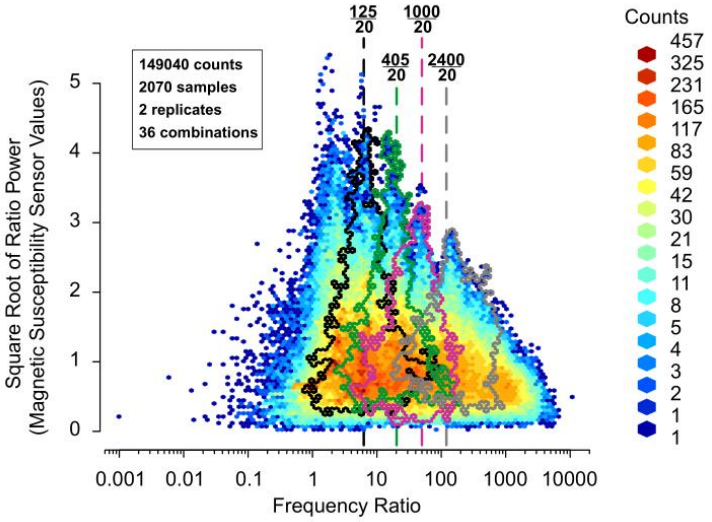

Figure SF18: Ratio population for all pairs of components of the decomposition of the magnetic susceptibility signal of ODP 926. The dotted lines stand for the expected frequency ratios. The black, green, purple and grey contours delineate the ratios of MSC3 with, respectively, MSC5 to 8.

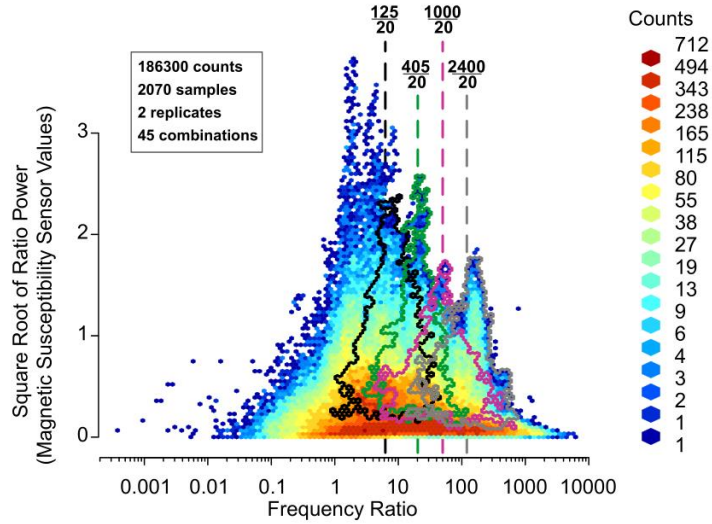

Figure SF19: Ratio population for all pairs of components of the amplitude demodulation of one realisation of MSC3 of the magnetic susceptibility signal of ODP 926 (see Figs. SF14 and SF15). The dotted lines stand for the expected frequency ratios. The black, green, purple and grey contours delineate the ratios of MSC3 with, respectively, the demodulation component corresponding to the 100, 400, 1000 and 2400 kyr (see fig. SF17).

The integrity of the raw decomposition is less than 10^{-15}, which is easily acceptable considering the range of values for the magnetic susceptibility signal. The parsimony of the raw decomposition is less than 2.2, which is slightly more than the parsimony for the greyscale signal decomposition (2.06). As these are two different signals, albeit of the same section, it is difficult to know if this difference has a concrete meaning.

The GZC departure values for the magnetic susceptibility signal are provided in Table ST3. The lower values are again found for the best expressed components, namely MSC 3 and MSC6. The highest values are found for the high frequency components, MSC 1 and 2. Untuned and tuned GZC departure values are roughly similar. The symmetry values for the components not having enough oscillations to compute the GZC departure are of 0.63 and 0.56 for MSC8, and of 0.80 and 0.75 for MSC9 (two values for each replicate). This is acceptable for MSC8, but raises questions about MSC9. This could be due to the low amplitude of MSC9, which makes it difficult to interpret as a meaningful sub-signal (e.g. Fig. SF16).

			20 kyr	**ca. 40 kyr**	**ca. 100 kyr**	**400 kyr**	**1000 kyr**
	MSC1	MSC2	MSC3	MSC4	MSC5	MSC6	MSC7
Untuned	1.36	1.42	1.25	1.28	1.24	1.12	1.26
Tuned	1.37	1.42	1.26	1.31	1.30	1.19	1.35

Table ST3: mean GZC departure for the Magnetic Susceptibility Components (MSC; see Figs. SF12 and SF13). The astronomical interpretation is provided (first line) when available. We compare it for both untuned (stratigraphic domain) and tuned (time domain, following the tuning interpretation of Wilkens et al., 2017) frequency computation.

The expression of the turbidite signalled in Figure 16 is less important in the magnetic susceptibility signal, compared to the greyscale one. Moreover, the turbidite is found exactly in a poorly sampled interval. The turbidite adds a wiggle in MSC 3, 4 and 5, and adds a few low-amplitude wiggles in the lower-frequency components.

References

Flandrin, P., Rilling, G., Goncalves. P., 2004. Empirical Mode Decomposition as a Filter Bank. IEEE Signal Proc. Lett. 11 (2): 112–114. https://doi.org/10.1109/LSP.2003.821662.

Hinnov, L.A., 2000. New Perspectives on Orbitally Forced Stratigraphy. Annu. Rev. Earth and Planet. Sci. 28 (1), 419–475. https://doi.org/10.1146/annurev.earth.28.1.419.

Huang, N.E., Wu, Z., Long, S.R., Arnold, K.C., Chen, X., Blank, K., 2009. On Instantaneous Frequency. Adv. Adapt. Data Anal. 01 (02): 177–229. https://doi.org/10.1142/S1793536909000096.

Laskar, J., Robutel, P., Joutel, F., Gastineau, M., Correia, A.C M., Levrard, B., 2004. A Long-Term Numerical Solution for the Insolation Quantities of the Earth. Astron. Astrophys. 428 (December): 261–285. https://doi.org/10.1051/0004-6361:20041335.

Laskar, J., Fienga, A., Gastineau, M., Manche, H., 2011. La2010: A New Orbital Solution for the Long Term Motion of the Earth. Astron. Astrophys. 532 (August): A89. https://doi.org/10.1051/0004-6361/201116836.

Mann, M.E., Lees, J.M., 1996. Robust Estimation of Background Noise and Signal Detection in Climatic Time Series. Clim. Chang. 33 (3): 409–445. https://doi.org/10.1007/BF00142586.

Meyers, S.R., 2014. Astrochron: An R Package for Astrochronology. https://cran.r-project.org/package=astrochron.

Olsen, P.E., Kent, D.V., 1999. Long-Period Milankovitch Cycles from the Late Triassic and Early Jurassic of Eastern North America and Their Implications for the Calibration of the Early Mesozoic Time–Scale and the Long–Term Behaviour of the Planets. Philos. Trans. Royal Soc. London. Series A: Math. Phys. Eng. Sci. 357 (1757), 1761–1786. https://doi.org/10.1098/rsta.1999.0400.

Rilling, G., Flandrin, P., Gonçalves, P., 2005. Empirical Mode Decomposition, Fractional Gaussian Noise and Hurst Exponent Estimation. In IEEE Int. Conf. on Acoust. Speech and Sig. Proc. Philadelphia, United States. IEEE. https://hal.inria.fr/inria-00570581.

Shackleton, N J., Crowhurst, S., 1997. Sediment Fluxes Based on an Orbitally Tuned Time Scale 5 Ma to 14 Ma, Site 926. In Hackleton, N.J., Curry, W.B., Richter, C., Bralower, T.J. (Eds.), Proceedings of the Ocean Drilling Program, Scientific Results, Vol. 154.

Sinnesael, M., De Vleeschouwer, D., Zeeden, C., Batenburg, S.J., Da Silva, A.-C., de Winter, N.J., Dinarès-Turell, J. et al. 2019. The Cyclostratigraphy Intercomparison Project (CIP): Consistency, Merits and Pitfalls. Earth Sci. Rev. 199 (December), 102965. https://doi.org/10.1016/j.earscirev.2019.102965.

Weedon, G.P. 2003. Time-Series Analysis and Cyclostratigraphy: Examining Stratigraphic Records of Environmental Cycles. Cambridge: Cambridge University Press.

Wilkens, R.H., Westerhold, T., Drury, A.J., Lyle, M., Gorgas, T., Tian, J., 2017. Revisiting the Ceara Rise, Equatorial Atlantic Ocean: Isotope Stratigraphy of ODP Leg 154 from 0 to 5 Ma. Clim. Past 13 (7), 779–793. https://doi.org/10.5194/cp-13-779-2017.

Zeeden, C., Hilgen, F., Westerhold, T., Lourens, L., Röhl, U., Bickert, T., 2013. Revised Miocene Splice, Astronomical Tuning and Calcareous Plankton Biochronology of ODP Site 926 between 5 and 14.4Ma. Palaeogeogr. Palaeoclimatol Palaeoecol. 369 (January): 430–451. https://doi.org/10.1016/j.palaeo.2012.11.009.